

**Superhard metallic compound TaB<sub>2</sub> via crystal orientation resolved strain stiffening**Chang Liu,<sup>1,2</sup> Xinlei Gu,<sup>3</sup> Kan Zhang<sup>Ⓢ,3,\*</sup>, Weitao Zheng,<sup>3</sup> Yanming Ma,<sup>1,2</sup> and Changfeng Chen<sup>Ⓢ,4,†</sup><sup>1</sup>*State Key Lab of Superhard Materials and International Center for Computational Method and Software, College of Physics, Jilin University, Changchun 130012, China*<sup>2</sup>*International Center of Future Science, Jilin University, Changchun 130012, China*<sup>3</sup>*State Key Laboratory of Superhard Materials, Key Laboratory of Automobile Materials, MOE, and Department of Materials Science, Jilin University, Changchun 130012, China*<sup>4</sup>*Department of Physics and Astronomy, University of Nevada, Las Vegas, Nevada 89154, USA*

(Received 7 September 2021; revised 2 December 2021; accepted 21 December 2021; published 10 January 2022)

We predict then produce superhard metallic compound TaB<sub>2</sub> via exploring crystal orientation resolved stress-strain relations. First-principles calculations identify prominent strain stiffening that generates superhigh indentation strengths of 46–49 GPa in the (001) oriented TaB<sub>2</sub> crystal; in sharp contrast, dynamic instability diminishes strain stiffening even causes softening, leading to notably lower strengths around 30 GPa in the (110) and (100) orientations. Ensuing experimental synthesis creates well crystallized and textured (001) oriented TaB<sub>2</sub> that exhibits indentation hardness of 45.9 GPa and electrical resistivity of  $1.71 \times 10^{-6} \Omega \text{ m}$ , validating key superhard and metallic benchmarks. The present findings showcase an enabling protocol of crystal configuration engineering for selective property optimization, opening a path for rational design and discovery of long-sought but hitherto scarcely produced superhard metallic materials among vast transition-metal compounds.

DOI: [10.1103/PhysRevB.105.024105](https://doi.org/10.1103/PhysRevB.105.024105)**I. INTRODUCTION**

Traditional superhard materials like diamond and cubic boron nitride (c-BN) play prominent roles in science and technology, but their applications are constrained by stringent synthesis conditions and performance limitations [1]. Recent years have seen the rise of a distinct class of strong materials comprising transition-metal (TM) and light elements [2–7], among which TM borides exhibit favorable synthesis conditions and properties [8–19]; however, many of these compounds suffer structural softening under large strains, rendering their hardness mostly in the 15–30 GPa range well below the 40 GPa threshold set for superhard materials [20–25]. A contrasting mechanism for strength enhancement via strain stiffening is uncommon among crystalline solids [26], but has been realized in selected cases like nanotwinned diamond and c-BN [27–30] and predicted in Mo<sub>2</sub>BC [31], offering an impetus for exploring TM compounds to find metallic superhard materials. Recent studies of TM borides have mostly focused on boron-rich compounds [8–14], but this strategy has been hampered by significant strain softening caused by boron's tendency to form the more deformable three-center bonding states [32]. Meanwhile, TM diborides host sufficient boron to form a strong covalent network while avoiding the vulnerable three-center bonding states, thus providing a promising material platform for exploring strain stiffening.

In this paper, we present computational prediction of superhard TaB<sub>2</sub> induced by conspicuous strain stiffening via a crystal orientation dependent strengthening mechanism, and then report on pertinent experimental validation by ensuring targeted synthesis and characterization. First-principles calculations of stress-strain relations uncover striking strain enhanced indentation strengths of 46–49 GPa in the (001) oriented TaB<sub>2</sub>, driven by the indentation induced elastic stiffening and bonding stabilization; in stark contrast, TaB<sub>2</sub> exhibits much lower indentation strengths around 30 GPa in the (110) and (100) orientations, constrained by the deformation triggered dynamic instability. Computed electronic density of states shows good metallicity in deformed TaB<sub>2</sub>. Guided by these findings, we have synthesized well crystallized and textured (001) oriented TaB<sub>2</sub> and performed nanoindentation and four-probe resistance measurements that produce intrinsic indentation hardness of 45.9 GPa and resistivity of  $1.71 \times 10^{-6} \Omega \text{ m}$ , validating key superhard and metallic characters. This integrated computational and experimental study opens a viable path of rational crystal orientation engineering to achieve mechanical properties far superior than corresponding aggregate quantities, which may significantly expand the scope of metallic superhard solids among TM compounds.

**II. COMPUTATIONAL AND EXPERIMENTAL METHODS****A. Computational details**

Stress-strain relations from first-principles calculations can accurately describe material deformation and strength under diverse loading conditions [33–43], and calculated

\*kanzhang@jlu.edu.cn

†chen@physics.unlv.edu

indentation strengths can be directly compared to well-controlled nanoindentation measurements [44–46]. Under indentation, shear instability usually precedes the initiation of cracks and dislocations [47], signaling the onset of incipient plasticity [36,38]. Indentation strength is determined by calculations under a biaxial stress that contains a shear ( $\sigma_{zx}$ ) and a normal compressive ( $\sigma_{zz}$ ) stress component that obey the relation  $\sigma_{zz} = \sigma_{zx} \tan \phi$ , where  $\phi$  is the centerline-to-face angle of the indenter [48,49]. We have performed calculations for a variety of TM carbides, nitrides, and borides, and the obtained indentation strengths accurately describe measured intrinsic indentation hardness [20–25]; multiaxial strains also produce versatile unusual structural, mechanical, and electronic properties [29,30,48–52]. We adopt this approach to assess strain stiffening in TaB<sub>2</sub>.

The first-principles calculations for electronic properties and stress-strain relations reported in this work have been carried out using the VASP code [53] adopting the projector augmented wave (PAW) approach [54] with the valence electron configurations of  $2s^2 2p^1$  and  $5p^6 5d^3 6s^2$  for boron and tantalum, respectively. The local density approximation (LDA) has been used to describe the exchange and correlation potential between electrons as parameterized by the Ceperley and Alder functional [55]. An energy cutoff of 800 eV and a Monkhorst-Pack grid [56] with a maximum spacing of  $0.18 \text{ \AA}^{-1}$  are adopted, achieving an energy convergence around 1 meV per atom with residual forces and stresses less than 0.005 eV/Å and 0.1 GPa, respectively. The lattice dynamical properties were calculated via the direct supercell method as implemented in the Phonopy code [57] with at least 144 atoms per cell.

Stress-strain relations under Berkovich loading conditions are calculated under a biaxial stress state that contains a shear stress and a normal compressive component. The shape of the deformed cell and atomic relaxation are determined completely at each step by the constrained structural optimization. The starting position for each strain step is taken from the relaxed coordinates of the previous strain step and with a small increment of 0.01 in each step to ensure the quasistatic strain path. At each step, the applied shear strain is fixed to determine the shear stress  $\sigma_{xz}$ , while the other five independent components of the strain tensors and all the atoms inside the cell are simultaneously relaxed until the normal stress component  $\sigma_{zz}$  reaches a specified value, namely  $\sigma_{zz} = \sigma_{xz} \tan \phi$  where  $\phi \sim 65^\circ$  corresponding to the prominent Berkovich shear stress state, or  $\sigma_{zz} \sim 0$  in pure shear case. Meanwhile, all other four components of the Hellmann-Feynman stress tensor and the force on each atom become negligibly small after the full relaxation, typically less than 0.1 GPa and 0.005 eV/Å, respectively.

## B. Experimental details

TaB<sub>2</sub> films were deposited in a direct current (DC) magnetron sputtering system using a 60-mm-diameter TaB<sub>4</sub> compound target (99.95%). The double-side polished Al<sub>2</sub>O<sub>3</sub>(0001) substrates ( $2 \times 2 \text{ cm}^2$ ) were ultrasonically cleaned in subsequent baths of acetone, alcohol, and deionized water for 20 min each, blown dry with nitrogen, and then mounted on the substrate-holder, inserted into the deposition

chamber. The target was facing the substrate holder at an 80-mm distance and from a  $45^\circ$  angle. The chamber was evacuated by mechanical pump and turbo molecular pump to a  $5 \times 10^{-4}$  Pa base pressure prior to sputtering. The 80 sccm Ar (99.999%) was introduced into the sputtering chamber to reach a constant working pressure of 0.8 Pa. Subsequently, the substrate temperature was set at a constant of  $600^\circ\text{C}$  and continuously detected by a pyrometer during the whole deposition process. To remove the surface oxide layer of target, Ar<sup>+</sup> ions were used to pre-sputtered etch the target for 10 minutes with a shutter shielding the substrate. Deposition was conducted at a DC-power of 200 W, a substrate bias voltage of  $-80 \text{ V}$ , and a substrate rotational speed of 10 r/min, respectively.

The crystal structure was determined by x-ray diffraction (XRD) using a Bragg-Brentano (Bruker D8) diffractometer in a  $\theta$ - $2\theta$  configuration with a monochromatic Cu K $\alpha$  source ( $\lambda = 0.15418 \text{ nm}$ ) as a source. A  $1^\circ$  divergent incident beam was produced, which was limited by an incident slit. The measurement was performed in locked coupled mode with 40 mA current, 40 kV voltage and a SMART APEX II CCD detector. The  $2\theta$ -value was calibrated using the substrate peak, which was set to the literature value of  $41.9^\circ$  at the measured positions of Al<sub>2</sub>O<sub>3</sub> (0001) reflection using Cu K $\alpha_1$  x-ray. The sample was placed on the plasticine in the pit of the tray, and then flattened by a glass plate from top to bottom. Readings were recorded at a scan-speed of 0.5 seconds/step in a  $2\theta$  range from  $20^\circ$  to  $60^\circ$ . The Jade 5.0 software with a PDF card database (2004 version) was utilized to analyze the XRD result.

The preferred orientation was assessed from XRD pole-figures recorded in a Rigaku Smartlab X-ray diffraction equipped with Cu K $\alpha$  resource operated at 40 kV and 30 mA. The (001) and (101) pole figures were both characterized by Schulz's reflection technique. The measurement was performed over the ranges of  $0^\circ < \psi < 81^\circ$  and  $0^\circ < \phi < 360^\circ$  with a scanning speed of  $5^\circ/\text{step}$ , where  $\psi$  was the sample rotation angle along the sample surface,  $\phi$  was the sample rotation angle along the normal direction of sample surface, respectively. To obtain the contour maps, the normalization was performed on the intensity of random orientation [58].

The high-resolution transmission electron microscope (HRTEM, JEOL 2010F), operated at 200 kV accelerating voltage, was utilized to further confirm the crystal structure of the samples. The sample powder was scraped off by sharp blades from the sample surface and was smeared on the Cu-microgrids. Subsequently, the Cu-microgrids were put into the vacuum chamber of microscope. The electron was focused by a freely regulated magnetic field, and obtain the clear images at 1 000 000 times magnifications. Subsequently, the HRTEM picture for TaB<sub>2</sub> film is imported in the DiffTools suite in DigitalMicrograph software, and the lattice spacing of TaB<sub>2</sub> film were measured.

In the nanoindentation test, the hardness  $H$  and elastic modulus  $E$  are calculated from the loading-unloading curve by the formulas [59]  $H = P_{\max}/A$  and  $E_r = (\sqrt{\pi}/2\beta)(S/\sqrt{A})$ , where  $P_{\max}$  is the maximum load obtained from loading-unloading curve,  $A$  is the contact area,  $\beta$  is a constant related to the indenter shape, and  $S$  is the slope of the top of unloading curve. The elastic modulus  $E_r$  represents the simultaneous

elastic deformation of film and indenter tip during the nanoindentation test, and is used to calculate the film  $E$  by the following equation [59]  $1/E_r = [(1 - \nu)/E + (1 - \nu_i^2)/E_i]$ , where  $\nu$  and  $E$  are the poisson ratio and elastic modulus for film, respectively. Besides,  $\nu_i$  and  $E_i$  are the poisson ratio ( $\nu = 0.07$ ) and elastic modulus ( $E_i = 1140$  GPa) for the indentation tip. Hence, by measuring the contact area  $A$ , one can calculate  $H$  and  $E$  by the above formulas. Up to now, the Oliver-Pharr method was widely used to estimate the  $A$  by fitting the relation between load ( $P$ ) and indentation tip displacement ( $h$ ) to an exponential function [60]  $P = B(h - h_f)^m$ , where  $B$  and  $m$  are fitting constants,  $h_f$  is the displacement of complete unloading.

The contact stiffness  $S$  was calculated by differentiating the first 25–50% part of unloading curve:  $S = (dP/dh)(h = h_{\max}) = Bm(h_{\max} - h_f)^{(m-1)}$ . Hence, the contact depth  $h_c$  is given by  $h_c = h_{\max} - \epsilon P/S$ , where  $\epsilon$  is a constant related to the indentation tip shape ( $\epsilon = 0.75$  for Berkovich). Furthermore,  $A$  is calculated by the empirical formula [60]  $A = f(h_c)$ . Hardness  $H$  of the films was evaluated by MTS Nanoindenter XP with continuous stiffness measurements (CSM) mode, in which stiffness is measured continuously during the loading of the indenter by imposing a small dynamic oscillation with a frequency of 45 Hz on the displacement signal and measuring the amplitude and phase of the corresponding force signal by means of a frequency-specific amplifier [61]. The CSM mode is an optional functional module of nanoindentation system, which is more suitable for testing the hardness of film samples. With a continuous measure of stiffness, we can obtain the hardness as a continuous function of depth from a single indentation experiment. That is, we can obtain the accurate hardness at a platform or peak value from the hardness-displacement curve, and this range is generally around 10% of film thickness which could avoid the surface effects [62] and the substrate effect [63]. In our nanoindentation test, the fused quartz standard of known hardness and elastic modulus was used as calibration [64], and a Berkovich pyramidal diamond probe with a nominal tip radius of 150 nm indented the sample to a maximum depth of 600 nm. Herein, the hardness for the samples was taken at approximately 50–120 nm depth. At least nine indentations at different places on the film surface were made to minimize the deviation of the results after rejecting few extreme values. The distance of each indentation was set at 30  $\mu\text{m}$  to avoid the effect of plastic deformation around the indentation [65].

The film thickness was observed by scanning electron microscope (SEM, JEOL JSM-6700F). The sample was adhered to the sample-stage by conductive adhesive and put into the vacuum chamber of microscope. The electron was focused by a freely regulated magnetic field, and then the high-quality pictures for film across-section was photographed at 2 kV high-voltage and 25 000 times magnification. According to the cross-sectional SEM, the sample thickness is estimated to be about 1.1  $\mu\text{m}$ .

The sheet resistance for the sample was characterized by a ST2253 four probe system with a linear 2-mm spacing arrangement of four tungsten carbide probes, and the measurement was repeated nine times for each sample. The film was cut into a square shape (length-width ratio = 1.0) to ensure the sheet resistance was accuracy. The electrical resistivity for the

sample was calculated by the following equation:  $\rho = R_s d$ , where  $\rho$ ,  $R_s$ , and  $d$  were electrical resistivity, sheet resistance and film thickness, respectively [66].

The electrical resistivity for the TaB<sub>2</sub> film is measured to be  $170.5 \pm 5.5 \mu\Omega \text{ cm}$ , characterizing the film as conductor [67]. This electrical resistivity is larger than the value for bulk TaB<sub>2</sub> samples ( $\sim 68 \mu\Omega \text{ cm}$ ) [68], which is a general feature for film samples attributed to the higher surface roughness and smaller grain size [69,70]. For films with large thicknesses ( $> 545$  nm), the scattering caused by surface roughness has a limited effect on the electrical resistivity [71]. Thus, in this paper, the higher electrical resistivity for the TaB<sub>2</sub> film with a thickness of about 1.1  $\mu\text{m}$  is mainly ascribed to the smaller grain sizes compare to bulk materials, which cause the increase of the electrical resistivity for the film [72].

### III. RESULTS AND DISCUSSIONS

Mechanical strength is usually described by elastic parameters, which are often taken as input for empirical formulas to generate a single aggregate hardness value. This widely used approach, however, does not account for anisotropic stress responses that make hardness sensitive to crystal orientation; moreover, elastic parameters of the crystal structure at equilibrium may not adequately describe bonding behaviors at large strains, where ultimate strength limits are determined. To unravel intricate mechanical processes and properties sensitive to strain and bonding states, we devise an integrated computational and experimental approach that first computes crystal-plane resolved stresses up to large strains reaching the elastic or dynamic stability limit to screen for prominent strain stiffening, then pursues synthesis in the targeted orientation for characterization. Here, we present an exemplary case study of TaB<sub>2</sub> that has a modest aggregate hardness but exhibits prominent directionally sensitive stress responses, leading to surprisingly superior hardness at the optimal (001) crystal orientation. This study raises fresh prospects for making superhard metallic materials among wide-ranging TM compounds.

At equilibrium TaB<sub>2</sub> adopts the hexagonal structure in  $P6/mmm$  symmetry [Fig. 1(a)], where each Ta atom is connected to twelve B atoms arranged in two parallel honeycomb layers, one on each side of the Ta atom, forming an hour-glass unit with the B-B and Ta-B bond lengths of 1.77 Å and 2.41 Å, respectively. Since a material's hardness is primarily determined by its ability to resist shear deformation [73], we examine shear stress responses of TaB<sub>2</sub> in its major low-index planes to establish key benchmarks. We show in Fig. 1(b) the stress responses under pure shear (PS) strains along the (001)[100] and (001)[210] slip directions, each of which is six-fold symmetric in the (001) plane [Fig. 1(a)]. The two sets of shear stresses reach peak values above 30 GPa; however, phonon calculations reveal that dynamic instabilities, indicated by the appearance of imaginary phonon modes [Fig. 1(e)], set in well below the elastic limits, reducing the maximal shear stresses to around 20 GPa. Analysis of the eigenvectors of the dynamic matrix indicates that the unstable phonon modes correspond to the vibrations with the Ta atoms moving along the directions of the Ta-B bonds that are most stretched thus weakened by the PS deformation [Fig. 1(g)].



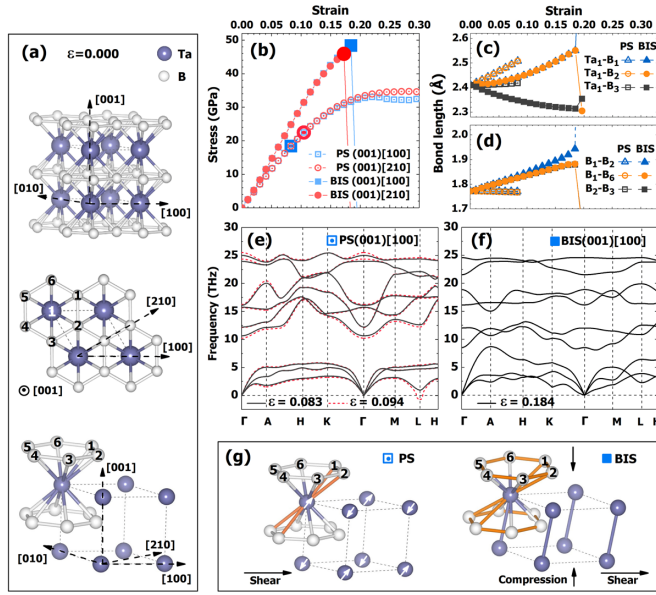


FIG. 1. (a) Crystal structure of  $\text{TaB}_2$  in 3D views and in the (001) plane. (b) Calculated stress responses to the indicated PS and BIS strains. Enlarged symbols mark the highest stress and strain values right before the onset of dynamic instability without reaching the elastic limits in the PS cases and at the elastic limits in the BIS case. [(c),(d)] Bond-length changes under the (001)[100] and (001)[210] PS and BIS strains. [(e),(f)] Calculated phonon dispersions at the (001)[100] PS (prior and post dynamic instability) and BIS (elastic limit) strains, and similar results at the (001)[210] PS and BIS strains are given in Fig. 2; (g) Atomic displacements of soft phonon modes under the (001)[100] PS strains in (e) and strengthened stable bonding patterns under the (001)[100] BIS strains in (f). Main load-bearing bonds are highlighted by thicker lines.

A pair of Ta-B bonds titled in each shear slip direction [see Figs. 1(c) and 1(g) for the PS (001)[100] results] are the main load bearers with the most quickly stretched bond lengths.

Hardness of strong solids is commonly measured by Berkovich or Vickers indenters with respective centerline-to-face angle  $\phi = 65.3^\circ$  and  $68^\circ$ , which produce similar results [74]. We use Berkovich indenter in this paper; thus, our theoretical analysis will focus on stress responses under Berkovich indentation shear (BIS) strains. For both major shear slip directions in the (001) plane, the calculated results [Fig. 1(b)] reveal more quickly rising BIS stresses that reach enhanced peak values of 46–49 GPa, which are about 50% higher than the corresponding PS peak stresses. This remarkable indentation strain stiffening stems from a load-induced switching of the main load-bearing bonds. Here the indentation induced normal compressive stress in the [001] direction constrains the elongation of the main load-bearing Ta-B bonds in the PS case [Fig. 1(c)]; meanwhile, the B-B bonds inside the boron honeycomb layers in the (001) plane are not constrained by the normal indentation stress, so they become the main load-bearing bonds with higher rates of elongation [Fig. 1(d)]. These stiffer boron bonds produce steeper and more pronounced stress responses, leading to the enhanced indentation strengths. Moreover, the normal stress compresses the Ta-Ta distance to 2.77 Å [Fig. 1(h)], which is smaller than the Ta-Ta bond length in Ta metal (2.88 Å). Crucially, these less

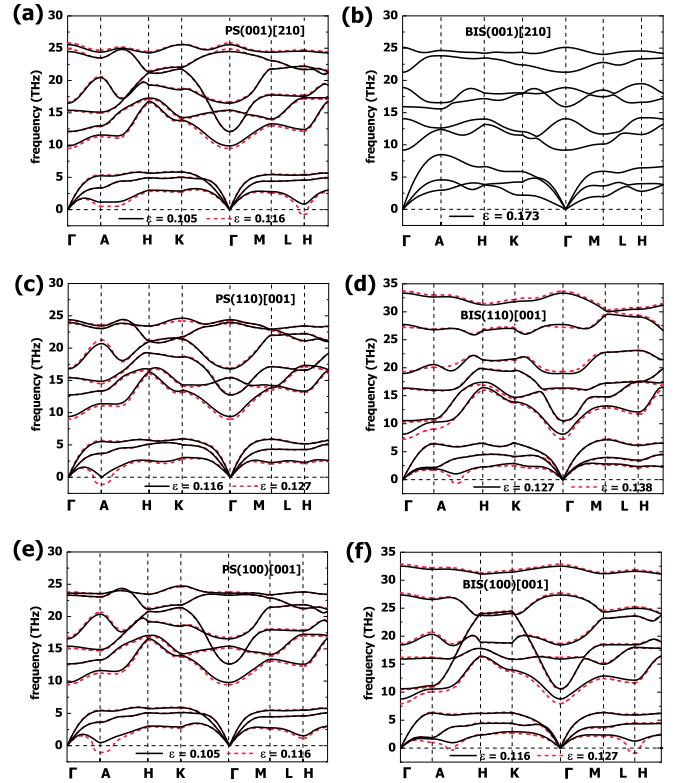


FIG. 2. Calculated phonon dispersion curves for the strained  $\text{TaB}_2$  under (a) the (001)[210] PS strains, (b) the (001)[210] BIS strains, (c) the (110)[001] PS strains, (d) the (110)[001] BIS strains, (e) the (100)[001] PS strains, and (f) the (100)[001] BIS strains. The results show the appearance of imaginary phonon modes under PS strains [as shown in (a), (c), and (e)] indicating the onset of dynamic instability of the deformed structure along the indicated deformation paths and the success [as shown in (b) at the elastic limit strain] or failure [as shown in (d) and (f)] of suppressing the dynamic instability under the corresponding BIS strains.

elongated and strengthened key Ta-B and Ta-Ta bonds combine to stabilize the  $\text{TaB}_2$  crystal and remove the dynamically unstable phonon modes [Fig. 1(f)]. Consequently, contrasting the PS case, the BIS stresses reach the much higher values set by the elastic limits [Fig. 1(b)]. Similar PS induced phonon softening and BIS strengthening are also observed under the (001)[210] strains (Fig. 2). With the six-fold bonding symmetry in the (001) plane [Fig. 1(a)], the two major shear slip modes span a dense, twelve-fold stiffened directions, making the (001) oriented  $\text{TaB}_2$  highly resistant to indentation deformation.

We now examine the (110) and (100) oriented  $\text{TaB}_2$ . Stress-strain calculations reveal notable indentation stiffening with BIS stresses reaching higher elastic limits than the PS peaks, similar to the (001) case, and the PS stresses are also reduced by dynamic instability [Figs. 3(a) and 3(e)], as indicated by the imaginary phonon modes [Figs. 3(b) and 3(f)], which stem from the deformation weakened bonds tilted in the PS slip directions [Figs. 3(d) and 3(h)]. Unlike the (001) case, however, BIS strains fail to constrain and stabilize the main load-bearing Ta-B bonds, because the normal stresses in the [110] and [100] indentation directions are not well aligned

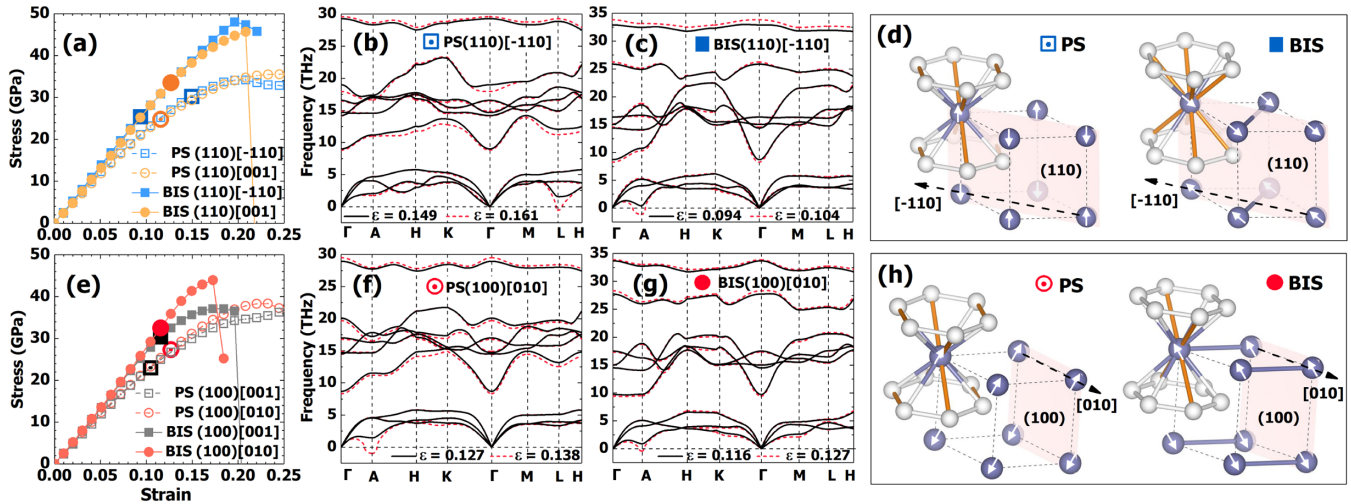


FIG. 3. [(a),(e)] Calculated stress responses to the indicated PS and BIS strains in the (110) and (100) planes. Enlarged symbols mark the data points with the highest stress and strain values right before the onset of dynamic instability. Calculated phonon dispersions right before and after the development of imaginary phonon modes under the [(b),(c)] (110)[-110] and [(f),(g)] (100)[010] PS and BIS strains, along with [(d),(h)] the associated soft-phonon atomic displacements. Phonon dispersions showing similar imaginary modes under the (110)[001] and (100)[001] PS and BIS strains are given in Fig. 2.

to compress the most vulnerable over-stretched Ta-B bonds that generate imaginary phonon modes [Figs. 3(c) and 3(g)] at similar strains, with comparable stresses, compared to the PS case [Figs. 3(a) and 3(e)]. The dynamic instability under the BIS strains greatly diminishes the range and magnitude of the elastic strengthening, resulting in only small increases or even a notable decrease (in the (110)[-110] slip direction) in the BIS strengths. These results underscore the sensitive nature of mechanical properties that vary substantially with changing crystal directions. Such orientation resolved stress responses shed light on hitherto largely unexplored material behaviors that can be exploited to tune strength and hardness that can notably exceed aggregate values, which are limited by the weaker structural and mechanical links that can now be identified and avoided via optimal crystal orientation selection.

Guided by the computational findings, we have pursued experimental synthesis and characterization of superhard metallic TaB<sub>2</sub> crystal in the (001) orientation using the magnetron sputtering technique, which is capable of producing selectively oriented specimens. Through extensive testing and optimization of synthesis conditions, we have obtained highly crystallized TaB<sub>2</sub> in the (001) orientation for experimental verification of the predicted superior mechanical property. The x-ray diffraction (XRD) pattern of the synthesized specimen [Fig. 4(a)] contains peaks at 27.7° and 56.5° that are attributed, respectively, to the (001) and (002) diffraction of the hexagonal crystal lattice of TaB<sub>2</sub>, while the peak at 41.9° is from the Al<sub>2</sub>O<sub>3</sub> substrate [75]. The full width at half maximum of the (001) peak is 0.44°, which yields, using the Scherrer formula [76], an estimated typical grain size around 20 nm in the specimen. The sharp (001) and (002) peaks indicate well crystallized and (001) orientated nature of the specimen. High-resolution transmission electron microscopy (HRTEM) imaging [Fig. 4(b)] provides direct evidence of excellent crystallinity of the synthesized TaB<sub>2</sub>. We performed pole-figure measurements to characterize the crystallographic

texture [77], and the results [Fig. 4(c)] show that the (001) pole-figure has a concentric ring of maximum intensity at the tilt angle  $\psi = 0^\circ$ , indicating the (001) orientation of the specimen; moreover, the (101) pole-figure has six high-intensity points separated by 60°, reflecting the six-fold symmetry of the P6/mmm structure, that locate at  $\psi = 60^\circ$ , which is the angle between the (001) and (101) planes of the TaB<sub>2</sub> crystal, corroborating the (001) orientation of the synthesized specimen.

We performed nanoindentation measurements using a Berkovich indenter in the continuous stiffness measurement (CSM) mode [61]. A typical CSM curve for the synthesized (001) TaB<sub>2</sub> is shown in Fig. 4(d) along with a calibration curve on the fused quartz standard. To extract the intrinsic hardness of the TaB<sub>2</sub> film, we followed the standard procedure taking data from the plateau region after the initial sharp rise and before the tapering off of the CSM curve to minimize the surface and substrate effects [62,63]. Measurements have been taken at nine different indentation spots on the specimen, giving an averaged hardness of  $45.9 \pm 1.0$  GPa. Highly crystallized and precisely oriented film specimens comprising grains sized 20 nm or larger are known to exhibit minimal grain-boundary effect and possess hardness close to that of high-quality single crystals [78]. So the measured result of 45.9 GPa can be regarded as a fair estimate of the intrinsic hardness of the (001) oriented TaB<sub>2</sub>, making it the first demonstrated native superhard material among TM compounds; moreover, the CSM curve stays consistently above 40 GPa for indenter displacement depths well into the tapering-off range, showcasing the robust superhard nature of the TaB<sub>2</sub> specimen. It is noted that nanoindentation is known to produce higher hardness than microindentation that involves more complicated plastic deformation modes, while the strain stiffening mechanism shown in this work is dominated by the strengthening in the elastic range, which is more closely related to the intrinsic bonding changes of the native crystal. We performed four-probe resistance measurements on

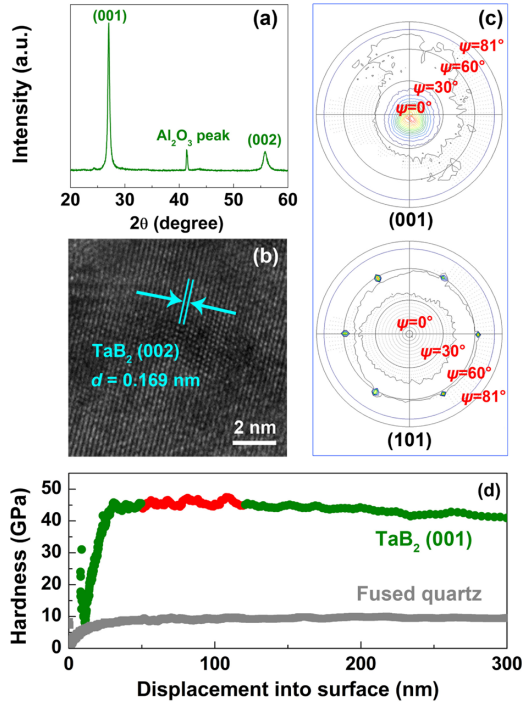


FIG. 4. Structural and mechanical characterization of TaB<sub>2</sub>. (a) The XRD pattern. (b) The HRTEM image, showing the 0.169 nm spacing between the (002) planes. (c) The contour plots of pole figures in the (001) and (101) planes with the stereographic projections across zenithal ( $\psi = 0 - 81^\circ$ ) and azimuthal ( $\phi = 0 - 360^\circ$ ) angles. (d) A typical nanoindentation curve as a function of indentation displacement. Results from a depth range of 50–120 nm (red symbols) are used to determine the intrinsic hardness. Also shown is a calibration curve on the standard fused quartz, well reproducing its known hardness of 10 GPa [64].

the (001) oriented specimen and obtained the resistivity of  $170.5 \pm 5.5 \times 10^{-8} \Omega \text{ m}$ , revealing its ample electrical conduction ability. We have calculated the electronic density of states near the Fermi energy for TaB<sub>2</sub> under all the examined PS and BIS strains, and the results all stay close to the value for the unstrained crystal (Fig. 5), indicating robust metallicity being well maintained under deformation.

Our findings elucidate crystal orientation sensitive strength enhancement by suppressing dynamic instability and promoting load-bearer switching, and these mechanisms are expected to be robust among TM diborides, raising the prospects that hitherto scarce superhard metallic compounds can be made via crystal orientation engineering among a much wider range of materials than previously believed. It is, however, possible that load-bearer switching and strain stiffening may not occur if the elastic or dynamic limit is reached at lower strains. More work is needed to sort out these intriguing scenarios to guide further exploration. Another promising route for further study is to probe ternary dual-TM diborides ( $M_xN_{1-x}$ )B<sub>2</sub> ( $M, N = \text{TM}$ ) that offer an extra degree (varying  $x$ ) for tuning the valence electron concentration and relative electronegativity that are known to impact mechanical properties [79]. This line of work may prove productive for probing a broad variety of TM borides, carbides and nitrides in search of more diverse orientation dependent superhard metallic compounds.

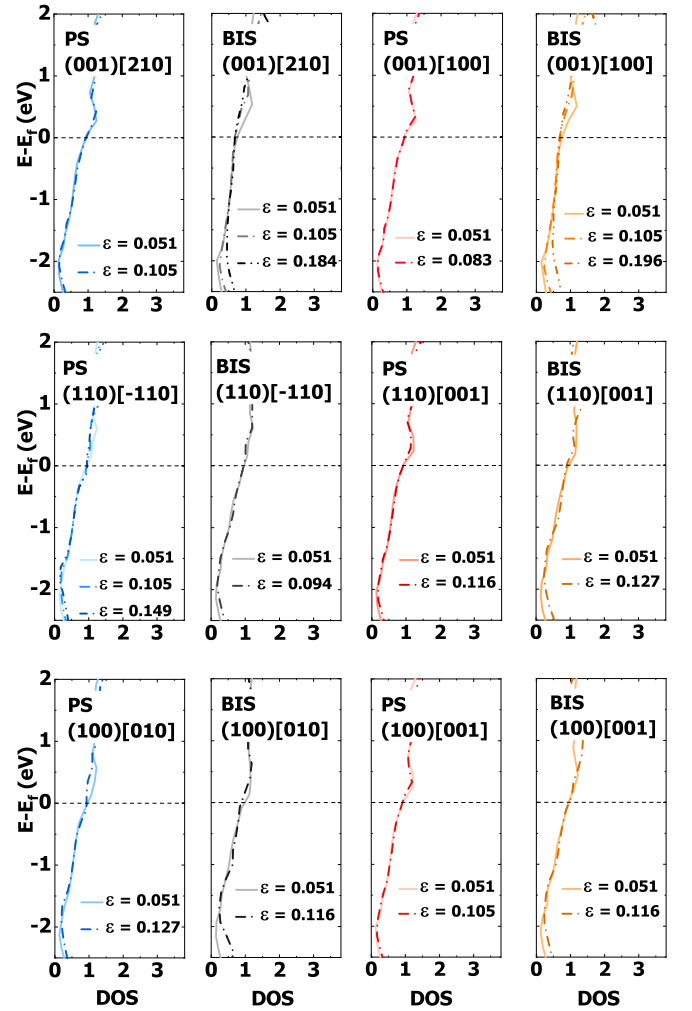


FIG. 5. Calculated electronic density of states (DOS) of TaB<sub>2</sub> under selected pure shear (PS) and Berkovich indentation shear (BIS) strains along the indicated shear slip directions. The results show that the DOS at the largest strain determined by the dynamic or elastic stability, whichever occurs first, in each case remains little changed in the strained crystal structures compared to the result for the crystal at equilibrium at  $\epsilon = 0$ , indicating robust metallicity of TaB<sub>2</sub> under diverse loading conditions examined in this work.

#### IV. SUMMARY

In summary, our concerted computational and experimental work on TaB<sub>2</sub> as an exemplary case study demonstrates that mechanical properties can be effectively modulated and optimized via exploring intricate crystal orientation resolved stress responses. First-principles calculations uncover prominent strain stiffening mechanisms that produce superior indentation strengths in the (001) oriented TaB<sub>2</sub>, while deformation induced dynamic instability limits the stress responses in the (110) and (100) orientations, resulting in notably reduced strengths. Ensuing experiments validate key superhard and metallic benchmarks in well crystallized and textured (001) oriented specimen. These results highlight a robust structural engineering approach for achieving orientation dependent mechanical properties that are superior to the corresponding aggregate results by identifying and



implementing the stronger while avoiding the weaker structural configurations. This approach may greatly expand the realm of superhard materials, especially allowing rational discovery of a distinct class of intrinsic superhard metallic materials among vast TM compounds. On a more general note, this paper shows that exploiting crystal orientation dependent structure-property relations opens an effective path for selectively tuning material behaviors that are sensitive to distinct bonding configurations.

## ACKNOWLEDGMENTS

This work was supported by the National Natural Science Foundation of China (Grant Nos. 51972139, 51602122, 51672101), National Key R&D Program of China (Grant No. 2016YFA0200400), the China Postdoctoral Science Foundation (Grant No. 2020M681031), the Program for JLU Science and Technology Innovative Research Team (2017TD-09) and the Fundamental Research Funds for the Central Universities.

- [1] V. V. Brazhkin, A. G. Lyapin, and R. J. Hemley, *Philos. Mag. A* **82**, 231 (2002).
- [2] E. Gregoryanz, C. Sanloup, M. Somayazulu, J. Badro, G. Fiquet, H. Mao, and R. J. Hemley, *Nat. Mater.* **3**, 294 (2004).
- [3] R. B. Kaner, J. J. Gilman, and S. H. Tolbert, *Science* **308**, 1268 (2005).
- [4] H. Y. Chung, M. B. Weinberger, J. B. Levine, A. Kavner, J. M. Yang, S. H. Tolbert, and R. B. Kaner, *Science* **316**, 436 (2007).
- [5] J. B. Levine, S. L. Nguyen, H. I. Rasool, J. A. Wright, S. E. Brown, and R. B. Kaner, *J. Am. Chem. Soc.* **130**, 16953 (2008).
- [6] Q. Gu, G. Krauss, and W. Steurer, *Adv. Mater.* **20**, 3620 (2008).
- [7] A. Friedrich, B. Winkler, L. Bayarjargal, W. Morgenroth, E. A. Juarez-Arellano, V. Milman, K. Refson, M. Kunz, and K. Chen, *Phys. Rev. Lett.* **105**, 085504 (2010).
- [8] R. W. Cumberland, M. B. Weinberger, J. J. Gilman, S. M. Clark, S. H. Tolbert, and R. B. Kaner, *J. Am. Chem. Soc.* **127**, 7264 (2005).
- [9] R. Mohammadi, A. T. Lech, M. Xie, B. E. Weaver, M. T. Yeung, S. H. Tolbert, and R. B. Kaner, *Proc. Natl. Acad. Sci. USA* **108**, 10958 (2011).
- [10] M. Xie, R. Mohammadi, Z. Mao, M. M. Armentrout, A. Kavner, R. B. Kaner, and S. H. Tolbert, *Phys. Rev. B* **85**, 064118 (2012).
- [11] M. Wang, Y. Li, T. Cui, Y. Ma, and G. Zou, *Appl. Phys. Lett.* **93**, 101905 (2008).
- [12] Q. Tao, D. Zheng, X. Zhao, Y. Chen, Q. Li, Q. Li, C. Wang, T. Cui, Y. Ma, X. Wang, and P. Zhu, *Chem. Mater.* **26**, 5297 (2014).
- [13] M. Xie, R. Mohammadi, C. L. Turner, R. B. Kaner, A. Kavner, and S. H. Tolbert, *Phys. Rev. B* **90**, 104104 (2014).
- [14] A. T. Lech, C. L. Turner, R. Mohammadi, S. H. Tolbert, and R. B. Kaner, *Proc. Natl. Acad. Sci. USA* **112**, 3223 (2015).
- [15] E. M. Carnicom, W. Xie, T. Klimczuk, J. Lin, K. Górnicka, Z. Sobczak, N. P. Ong, and R. J. Cava, *Sci. Adv.* **4**, eaar7969 (2018).
- [16] J. Wang, T. N. Ye, Y. Gong, J. Wu, N. Miao, T. Tada, and H. Hosono, *Nat. Commun.* **10**, 2284 (2019).
- [17] P. R. Jothi, K. Yubuta, and B. P. Fokwa, *Adv. Mater.* **30**, 1704181 (2018).
- [18] G. Akopov, M. T. Yeung, and R. B. Kaner, *Adv. Mater.* **29**, 1604506 (2017).
- [19] W. Gong, C. Liu, X. Song, Q. Li, Y. Ma, and C. Chen, *Phys. Rev. B* **100**, 220102(R) (2019).
- [20] C. Zang, H. Sun, and C. F. Chen, *Phys. Rev. B* **86**, 180101(R) (2012).
- [21] C. Zang, H. Sun, J. S. Tse, and C. F. Chen, *Phys. Rev. B* **86**, 014108 (2012).
- [22] B. Li, H. Sun, C. Zang, and C. F. Chen, *Phys. Rev. B* **87**, 174106 (2013).
- [23] B. Li, H. Sun, and C. F. Chen, *Phys. Rev. B* **90**, 014106 (2014).
- [24] H. Wu, H. Sun, and C. F. Chen, *Appl. Phys. Lett.* **105**, 211901 (2014).
- [25] Q. Li, D. Zhou, W. Zheng, Y. Ma, and C. F. Chen, *Phys. Rev. Lett.* **115**, 185502 (2015).
- [26] C. Jiang and S. G. Srinivasan, *Nature (London)* **496**, 339 (2013).
- [27] Y. Tian, B. Xu, D. Yu, Y. Ma, Y. Wang, Y. Jiang, W. Hu, C. Tang, Y. Gao, K. Luo *et al.*, *Nature (London)* **493**, 385 (2013).
- [28] Q. Huang, D. Yu, B. Xu, W. Hu, Y. Ma, Y. Wang, Z. Zhao, B. Wen, J. He, Z. Liu, and Y. Tian, *Nature (London)* **510**, 250 (2014).
- [29] B. Li, H. Sun, and C. F. Chen, *Nat. Commun.* **5**, 4965 (2014).
- [30] B. Li, H. Sun, and C. F. Chen, *Phys. Rev. Lett.* **117**, 116103 (2016).
- [31] A. Mansouri Tehrani, A. Lim, and J. Brgoch, *Phys. Rev. B* **100**, 060102(R) (2019).
- [32] W. Zhou, H. Sun, and C. Chen, *Phys. Rev. Lett.* **105**, 215503 (2010).
- [33] R. H. Telling, C. J. Pickard, M. C. Payne, and J. E. Field, *Phys. Rev. Lett.* **84**, 5160 (2000).
- [34] H. Chacham and L. Kleinman, *Phys. Rev. Lett.* **85**, 4904 (2000).
- [35] S. H. Jhi, S. G. Louie, M. L. Cohen, and J. W. Morris, Jr., *Phys. Rev. Lett.* **87**, 075503 (2001).
- [36] S. Ogata, J. Li, and S. Yip, *Science* **298**, 807 (2002).
- [37] D. M. Clatterbuck, C. R. Krenn, M. L. Cohen, and J. W. Morris, Jr., *Phys. Rev. Lett.* **91**, 135501 (2003).
- [38] S. Ogata, J. Li, N. Hirotsaki, Y. Shibutani, and S. Yip, *Phys. Rev. B* **70**, 104104 (2004).
- [39] X. Blase, P. Gillet, A. San Miguel, and P. Mélinon, *Phys. Rev. Lett.* **92**, 215505 (2004).
- [40] Y. Zhang, H. Sun, and C. F. Chen, *Phys. Rev. Lett.* **93**, 195504 (2004).
- [41] Y. Zhang, H. Sun, and C. F. Chen, *Phys. Rev. Lett.* **94**, 145505 (2005).
- [42] Y. Zhang, H. Sun, and C. F. Chen, *Phys. Rev. B* **73**, 144115 (2006).
- [43] M. G. Fyta, I. N. Remediakis, P. C. Kelires, and D. A. Papaconstantopoulos, *Phys. Rev. Lett.* **96**, 185503 (2006).
- [44] C. R. Krenn, D. Roundy, Marvin L. Cohen, D. C. Chrzan, and J. W. Morris, Jr., *Phys. Rev. B* **65**, 134111 (2002).
- [45] M. I. Eremets, I. A. Trojan, P. Gwaze, J. Huth, R. Boehler, and V. D. Blank, *Appl. Phys. Lett.* **87**, 141902 (2005).
- [46] T. Li, J. W. Morris, Jr., N. Nagasako, S. Kuramoto, and D. C. Chrzan, *Phys. Rev. Lett.* **98**, 105503 (2007).

- [47] A. Gouldstone, H. J. Koh, K. Y. Zeng, A. E. Giannakopoulos, and S. Suresh, *Acta Mater.* **48**, 2277 (2000).
- [48] Z. C. Pan, H. Sun, and C. F. Chen, *Phys. Rev. Lett.* **98**, 135505 (2007); **98**, 149905(E) (2007).
- [49] Z. Pan, H. Sun, Y. Zhang, and C. Chen, *Phys. Rev. Lett.* **102**, 055503 (2009).
- [50] C. Liu, X. Song, Q. Li, Y. Ma, and C. Chen, *Phys. Rev. Lett.* **123**, 195504 (2019).
- [51] C. Liu, X. Song, Q. Li, Y. Ma, and C. Chen, *Phys. Rev. Lett.* **124**, 147001 (2020).
- [52] C. Liu, X. Song, Q. Li, Y. Ma, and C. Chen, *Chin. Phys. Lett.* **38**, 086301 (2021).
- [53] G. Kresse and J. Furthmüller, *Phys. Rev. B* **54**, 11169 (1996).
- [54] G. Kresse and D. Joubert, *Phys. Rev. B* **59**, 1758 (1999).
- [55] D. M. Ceperley and B. J. Alder, *Phys. Rev. Lett.* **45**, 566 (1980).
- [56] H. J. Monkhorst and J. D. Pack, *Phys. Rev. B* **13**, 5188 (1976).
- [57] A. Togo and I. Tanaka, *Scr. Mater.* **108**, 1 (2015).
- [58] K. H. Brosnan, G. L. Messing, R. J. Meyer, and M. D. Vaudin, *J. Am. Ceram. Soc.* **89**, 1965 (2006).
- [59] H. Ljungcrantz, M. Odén, L. Hultman, J. E. Greene, and J. E. Sundgren, *J. Appl. Phys.* **80**, 6725 (1996).
- [60] J. Tong, Y. R. Zhao, J. Y. Sun, and D. H. Chen, *J. Mater. Sci.* **42**, 2894 (2007).
- [61] J. Hay, P. Agee, and E. Herbert, *Exp. Techniques* **34**, 86 (2010).
- [62] M. S. Bobji, S. K. Biswas, and J. B. Pethica, *Appl. Phys. Lett.* **71**, 1059 (1997).
- [63] X. D. Li, H. S. Gao, C. J. Murphy, and K. K. Caswell, *Nano Lett.* **3**, 1495 (2003).
- [64] W. C. Oliver and G. M. Pharr, *J. Mater. Res.* **7**, 1564 (1992).
- [65] W. Zhang and G. Subhash, *Acta Mater.* **49**, 2961 (2001).
- [66] F. M. Smits, *Bell Syst. Tech. J.* **37**, 711 (1957).
- [67] M. Trojanowska-Tomczak, R. Steller, J. Janukiewicz, J. Ziája, and G. Szafran, *J. Appl. Polym. Sci.* **129**, 3536 (2013).
- [68] C. C. Wang, S. A. Akbar, W. Chen, and V. D. Patton, *J. Mater. Sci.* **30**, 1627 (1995).
- [69] V. Timoshevskii, Y. Q. Ke, H. Guo, and D. Gall, *J. Appl. Phys.* **103**, 113705 (2008).
- [70] P. Y. Zheng, T. Zhou, B. J. Engler, J. S. Chawla, R. Hull, and D. Gall, *J. Appl. Phys.* **122**, 095304 (2017).
- [71] N. C. Zoita, V. Braic, M. Danila, A. M. Vlaicu, C. Logofatu, C. E. A. Grigorescu, and M. Braic, *J. Cryst. Growth* **389**, 92 (2014).
- [72] B. O. Johansson, J. E. Sundgren, J. E. Greene, A. Rockett, and S. A. Barnett, *J. Vac. Sci. Technol. A* **3**, 303 (1985).
- [73] D. M. Teter, *Mater. Res. Bull.* **23**, 22 (1998).
- [74] N. A. Sakharova, J. V. Fernandes, J. M. Antunes, and M. C. Oliveira, *Int. J. Solids Struct.* **46**, 1095 (2009).
- [75] B. D. Ozsdolay, C. P. Mulligan, K. Balasubramanian, L. P. Huang, S. V. Khare, and D. Gall, *Surf. Coat. Technol.* **304**, 98 (2016).
- [76] U. Holzwarth and N. Gibson, *Nat. Nanotechnol.* **6**, 534 (2011).
- [77] R. J. Roe, *J. Appl. Phys.* **36**, 2024 (1965).
- [78] C. H. Ma, J. H. Huang, and H. Chen, *Surf. Coat. Technol.* **200**, 3868 (2006).
- [79] X. L. Gu, C. Liu, H. Guo, K. Zhang, and C. F. Chen, *Acta Mater.* **207**, 116685 (2021).